Rare Metal Materials and Engineering
Volume 54, Issue 9, September 2025
Available online at www.rmme.ac.cn

Science Press

Cite this article as: Jiang Shihui, Di Jinnan, Xu Zaidong, et al. Near β Titanium Alloy with High Strength Obtained by Composition Design and Intermediate Annealing Process[J]. Rare Metal Materials and Engineering, 2025, 54(09): 2211-2219. DOI: https://doi.org/10.12442/j.issn.1002-185X.20240453.

ARTICLE

Near β Titanium Alloy with High Strength Obtained by Composition Design and Intermediate Annealing Process

Jiang Shihui[1], Di Jinnan[2], Xu Zaidong[3], Sun Saihua[3], Mao Pingli[1]

[1] School of Materials Science and Engineering, Shenyang University of Technology, Shenyang 110870, China; [2] Guidaojiaotong Polytechnic Institute, Shenyang 110230, China; [3] Northeastern University, Shenyang 110000, China

Abstract: A near β-type Ti-5.5V-4Mo-2.2Cr-Fe-3.6Al alloy was designed based on the multi-alloying principle of critical composition, combined with parameters, such as electron concentration, molybdenum equivalent and B_o-M_d, that can influence the stability of β phase. The homogenized alloy was subjected to solid solution, intermediate annealing during the rolling process, and aging treatment. The microstructure and mechanical properties of the alloy were analyzed by optical microscope, scanning electron microscope, X-ray diffractometer, electron backscattered diffraction and transmission electron microscope, as well as room-temperature tensile properties. The results show that martensitic transformation occurs in the alloy during rolling. The grain size of the alloy after intermediate annealing is only 38 μm, because the martensite is a hindrance to grain boundary migration. Grain refinement endows the annealed alloy with a good match of strength and plasticity, a yield strength of 1050 MPa and an elongation of 15%. A large number of α phases are precipitated in the microstructure of the rolled alloy after aging treatment, which further improves the properties of the alloy: the strength of the alloy exceeds 1500 MPa and the elongation is 5%.

Key words: near β titanium alloy; cold rolling; annealing; tensile properties

1 Introduction

Titanium alloys are widely used in aerospace, automotive and other important industrial fields due to their high strength and good corrosion resistance[1–7]. Among them, the β-type titanium alloy has good plasticity in the solid solution state, and has ultra-high specific strength and good corrosion resistance after aging, which is attractive to the material research field. Now, it has been applied to the structural parts of large aircrafts, for example, Ti-1023 (Ti-10V-2Fe-3Al) alloy and Ti55531 (Ti-5Al-5Mo-5V-3Cr-1Zr) alloy[9–12]. Specifically, for near β titanium alloy, due to its critical composition and good aging precipitation ability, the alloy can obtain a strengthening effect of 400–700 MPa after aging[13–17]. Zhang et al[18] showed that the volume fraction of α phase in near β titanium alloy after aging treatment was high, about 42%–80%, the average size was 35–150 nm, and a large number of fine α phases increased the strength to 1600 MPa. With the rapid development of the aerospace industry, the demand for the service strength of titanium alloys is increasing, and the performance of titanium alloys is further improved. The properties of the alloy are improved from the perspective of composition design and heat treatment process in this study.

The composition design of near β titanium alloys generally adopts the principle of diversification of critical composition. Under the condition that the molybdenum equivalent ($[Mo]_{eq}$) of the alloy is the critical value, several β-type stabilizing elements (V, Mo, Cr and Fe) and α-type stabilizing element (Al) are added appropriately. Li et al[19] designed Ti-5.2Mo-5.2Cr-4.0Al-4.4V-2.4Nb alloy based on this concept, whose strength can reach 1560 MPa after aging. Coffgniiez et al[20] designed a metastable β-type titanium alloy using electronic parameters such as bond order (B_o) and metal d-orbital energy level (M_d), the alloy has a good performance. This indicates that $[Mo]_{eq}$ and electronic parameters such as B_o and M_d can effectively predict the stability of β phase after aging. Therefore, according to the design method above, a near β

Received date: August 25, 2024
Foundation item: 14th Five-Year Plan of Liaoning Province Education Science (JG22EB103)
Corresponding author: Mao Pingli, Ph. D., Professor, School of Materials Science and Engineering, Shenyang University of Technology, Shenyang 110870, P. R. China, Email: PLMao@sut.edu.cn

-type titanium alloy with a nominal composition of Ti-5.5V-4Mo-2.2Cr-1Fe-3.6Al (wt%) was designed in this work. At the same time, the electronic parameters such as electron concentration, B_o and M_d of the alloy were considered. The nominal composition is Ti-5V-2Mo-2Cr-1Fe-6Al (at%).

The β phase in the near β-type titanium alloy is more metastable than that in the metastable β-type titanium alloy, and the martensitic transformation is easy to occur during the deformation process, which can increase the hardening rate of the alloy during the deformation process. At the same time, the generation of martensite is also conducive to grain refinement during annealing, and it can synergistically improve the strength and plasticity of the alloy. Therefore, cold rolling combined with annealing process was used to refine the grain of the alloy. Zhang et al[21] prepared a high-strength β-type titanium alloy by cold rolling and annealing treatment. According to the experience of related rolling and heat treatment processes, the effects of annealing after different cold rolling deformations, single annealing and intermediate annealing processes on the microstructure of the alloy were compared in this study, and the related processes for obtaining fine β grain structure were explored.

Combined with the above research, a new near β-type Ti-5.5V-4Mo-2.2Cr-1Fe-3.6Al (wt%) alloy was designed according to the $[Mo]_{eq}$ and electronic parameters, such as electron concentration and B_o-M_d in this study, and the alloy was subjected to intermediate annealing during rolling and aging treatment. It provides a reference for the composition design of near β-type titanium alloy and the synergistic improvement of strength and plasticity by rolling and heat treatment.

2 Experiment

Commercial metastable β-type titanium alloys with good properties generally contain elements V, Mo, Cr and Fe, such as Ti-1023 (Ti-10V-2Fe-3Al) alloy and Ti55531 (Ti-5Al-5V-5Mo-3Cr-1Zr) alloy. V and Mo are β phase stable elements of the same crystal type, and they are infinitely miscible with Ti in the crystals of bcc and hcp structures. Therefore, there is no clear constraint on the content of V and Mo in the alloy composition design. In order to avoid the formation of $TiCr_2$ intermetallic compound during the aging process, Cr addition is generally not more than 3%, because it is a slow eutectoid element. As Fe is a fast eutectoid element, it is easy to produce compounds such as TiFe and $TiFe_2$ during the aging process. And the segregation of element Fe is also easy to cause β spots, so the addition amount should be less than or equal to 2%. In addition, in order to improve the precipitation ability of α phase and avoid the generation of precipitate-free zones at grain boundaries, 3% of Al is generally added to titanium alloy. Based on the above factors, in order to give full play to the alloying effect of each element, the alloy composition design comprehensively selects elements such as V, Mo, Cr, Fe and Al.

$[Mo]_{eq}$, valence electron concentration (VEC) and B_o-M_d are all related to the structural stability and final properties of metastable β-type titanium alloys. They are also the most commonly used parameters in the composition design of metastable β-type titanium alloys. They can be used as conditions to constrain the content of components and further determine the element content of the alloy. When the $[Mo]_{eq}$ is close to the critical value of 10, the stability of the β phase is considered to be the lowest, and the alloy has the strongest aging precipitation ability. Therefore, the value of 10 should be taken as the target $[Mo]_{eq}$. The calculation formula of $[Mo]_{eq}$ is expressed as follow:

$$[Mo]_{eq}=1.0Mo+0.67V+0.44W+0.28Nb+0.22Ta+2.9Fe+1.6Cr+1.54Mn+1.25Ni-1.0Al\ (wt\%) \quad (1)$$

Since VEC is related to the structural stability of titanium alloys and the properties of the β phase, it has been confirmed by a large number of experiments[19–22]. Therefore, in the process of composition design, VEC is also considered to be one of the physical parameters affecting the stability of β phase in Ti alloy. Similiar to the $[Mo]_{eq}$, the structural stability of the β-phase solid solution is low when the VEC value is small. Twinning and phase transformation are easy to occur during the tensile process to increase the hardening rate of the alloy deformation, which also helps to improve the toughness of the alloy. Therefore, this study selected VEC value as 4.10. VEC is expressed in Eq. (2), as follows:

$$\frac{e}{a}=\sum_{i=1}^{n}X_iN_i \quad (2)$$

where e is the total number of valence electrons; a is the total number of atoms in the alloy; X_i (i=1, 2, 3, 4) represents the molar concentration of elements; N_i is the number of valence electrons of each element. In recent years, some studies have used the B_o-M_d parameter to predict the phase composition and deformation mechanism of titanium alloys. B_o is used to reflect the strength of covalent bonds formed between Ti and alloying elements, and M_d is a parameter closely related to the electronegativity of the element and the radius of the metal bond[23]. Fig.1 is a B_o-M_d phase diagram showing the (B_o, M_d) position of the designed alloy. When the (B_o, M_d) value is between the martensitic transformation line (M_d=room temperature (RT)) induced by stress and the martensitic transformation start line (M_s=RT) at RT, the alloy has better mechanical properties. At this time, the (B_o, M_d) position of the alloy is close to that of the commercial near β titanium alloy Ti-10V-2Fe-3Al. Therefore, the target (B_o, M_d) position is selected as (2.773, 2.361), which is close to that of Ti-1023. The calculation formulas of B_o and M_d values are as follows:

$$\overline{B}_o=\sum_{i=1}^{n}X_i\,(B_o)_i \quad (3)$$

$$\overline{M}_d=\sum_{i=1}^{n}X_i(M_d)_i \quad (4)$$

where $(B_o)_i$ is the B_o value of element i, $(M_d)_i$ is the M_d value of element i. The positions of (B_o, M_d) of the alloy and some near-β-type alloys with good properties can be marked through calculation, in the stable phase diagrams of $\overline{B}_o$ and $\overline{M}_d$ values, as shown in Fig.1.

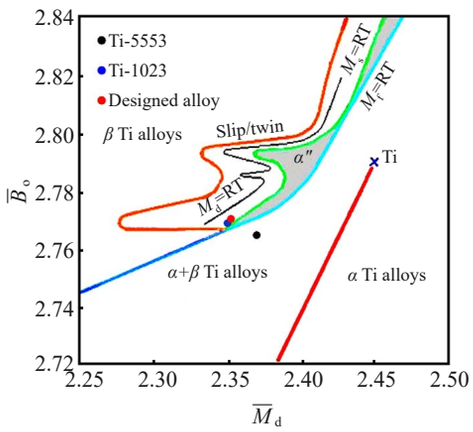

Fig.1 $\overline{B}_o$-$\overline{M}_d$ two-parameter diagram

According to Eq. (1 – 4) and $\sum_{i=1}^{n} C_i = 1$, the nominal composition of the alloy can be calculated as Ti-5.5V-4Mo-2.2Cr-1Fe-3.6Al (wt%). Table 1 shows the actual composition of the alloy, and the error between each component and the nominal component is less than 1.5%.

The alloys were prepared using the raw metals of Ti, V, Mo, Cr, Fe and Al with purities exceeding 99.9%, and were prepared through arc-melting for more than six times in an argon atmosphere. Subsequently, all the ingots (300 g in mass) were homogenized in a vacuum at 1000 ℃ for 24 h, followed by water quenching (WQ). The elements of V, Mo, Cr, Fe and Al in the alloy were determined by infrared analysis. The oxygen content in the alloy was determined by pulse heating inert gas melting infrared absorption method. The homogenized alloy ingot was cut into cuboid samples using electro-discharge machining. The cuboid sample was treated by solid solution and used as the original sample for cold rolling. The phase transition point of the alloy was 840 °C measured by metallographic method. In order to avoid the formation of α precipitation phase in the annealing process, the temperature in the intermediate annealing process during the rolling process was selected as 870 °C above the phase transition point, and the annealing time was 30 min. The process flow diagram of the intermediate annealing process used in this study is shown in Fig.2.

Samples were mechanically ground and polished, and then etched with a solution (10% HF+30% HNO_3+60% H_2O). Microstructures were characterized via optical microscope (OM, Olympus-PMG3) and scanning electron microscope (SEM, Zeiss Sigma) coupled with electron backscatter diffraction (EBSD) and energy-dispersive X-ray spectroscope (EDS). Additionally, sub-microstructures were characterized via transmission electron microscope (TEM, JEM-2100F). X-ray diffraction (XRD) was applied to identify phases in the

Table 1 Chemical composition of the designed alloy (wt%)

V	Mo	Cr	Fe	Al	C	O	H	Ti
5.56	3.97	2.33	1.04	3.04	<0.10	0.11	<0.10	Bal.

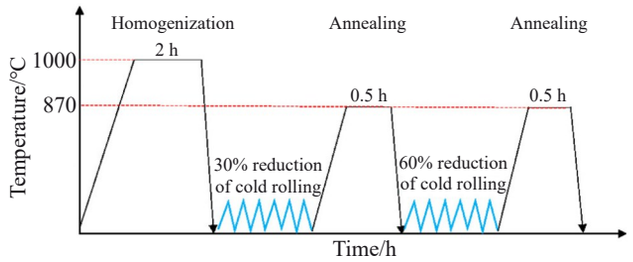

Fig.2 Process flow diagram of intermediate annealing during rolling process

alloys by using a SmartLab(9) diffraction instrument with an incident beam of Cu-Kα radiation. Scanning was performed from 20° to 100° at a scanning rate of 5°/min. SEM samples were initially polished by 3000# SiC papers, and then electrochemically polished for the final surface clarification using a solution composed of methanol, n-butanol, ethylene glycol butyl ether, and perchloric acid (6.5:2:1:0.5) at a direct voltage of 25 V and a temperature of about 253 K. TEM samples were punched to Φ3 mm plate sheets and then mechanically ground to 55 μm in thickness, and finally subjected to twin-jet electro-polishing using a solution of $HClO_4$: C_2H_6O=1: 8 at the temperature of about 248 K. The tensile tests were conducted on a CMT-5305GL universal electronic tensile testing machine with a strain rate of 1×10^{-3} s^{-1} at RT. Three samples of each alloy were used to determine the tensile properties, and the averaged values were adopted.

3 Results

Fig.3a shows that the microstructure of the as-cast alloy has coarse grains with strip-shaped α precipitates distributed within the grains. Due to the low-melting-point alloying elements, such as Al being prone to segregation at grain boundaries, α phases are prone to precipitate at grain boundaries, which can cause brittle fracture of the alloy during deformation. Therefore, it is necessary to eliminate element segregation by homogenization. Fig. 3b and Fig. 3c show OM and SEM images of the alloy after homogenization at 1000 °C/2 h, respectively, which indicate that the α phase present in the as-cast state has been dissolved into the matrix. XRD results in Fig. 3b also demonstrate that only a single bcc structure remains after homogenization. SEM-EDS results indicate that the distribution of various alloying elements in the alloy after homogenization is uniform, which is beneficial for the uniform distribution of α phase after aging.

Fig. 4 presents XRD patterns of the alloy after cold rolling with different reductions. The microstructure of the alloy after cold rolling with a 30% reduction is entirely composed of a single bcc structure. After increasing the cold rolling reduction to 60%, in addition to the β matrix, hexagonal martensite phase precipitates in the microstructure, which increases the hardening rate in cold rolling process and hinders further cold rolling deformation. Fig. 5 shows the OM images of samples with different cold rolling reductions and the OM images of recrystallized samples after annealing at 870 °C/30 min, as

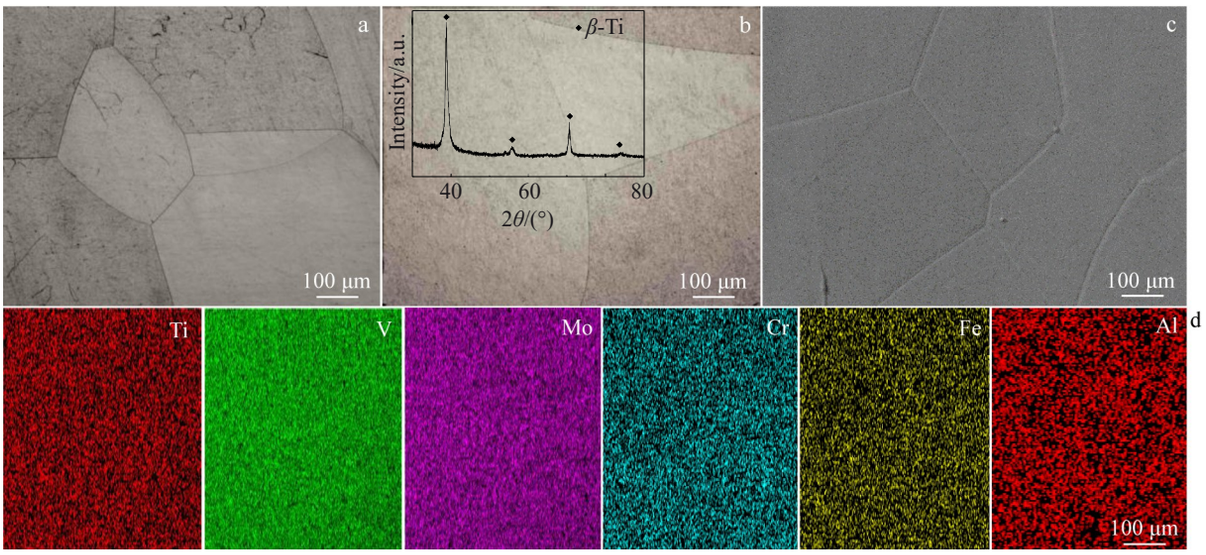

Fig.3 OM image of as-cast alloy (a); OM image and XRD pattern of homogenized alloy (b); SEM image (c) and corresponding EDS results (d) of homogenized alloy

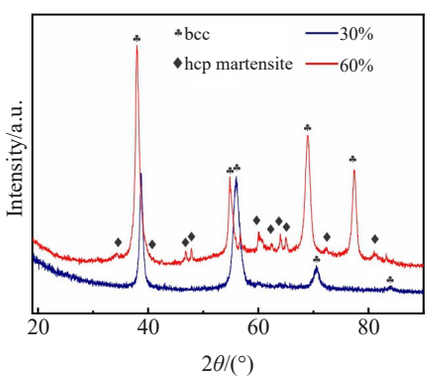

Fig.4 XRD patterns of the alloy after cold rolling with 30% and 60% reductions

well as the corresponding inverse pole figure (IPFs). Fig. 5a shows that the grain size of the alloy remains almost unchanged after cold rolling with a 30% reduction, and a large number of slip lines appear inside the grains. However, the internal deformation of the alloy is uneven, and the number of slip lines generated inside different grains varies greatly. After annealing and recrystallization, the grain refinement of the alloy is relatively small. According to IPFs, the grain size of the alloy after annealing is approximately 150 μm. Fig. 5b shows that the grains undergo a certain degree of deformation after cold rolling with a 60% reduction, and the grains after annealing and recrystallization are relatively uniform. According to IPF image, the average grain size of the alloy after 60% cold rolling and annealing is about 75 μm. The microstructure of the alloy after secondary cold rolling with 60% reduction and annealing after cold rolling is shown in Fig. 5c, where smaller grains undergo a certain amount of deformation. After annealing and recrystallization, the grains are further refined. According to IPFs, the average grain size of the alloy is 38 μm.

Fig.6 presents TEM bright field (BF) image, dark field (DF) image, and corresponding selected area electron diffraction (SAED) patterns after cold rolling with a 60% reduction. SAED pattern of the corresponding blue circle area in Fig. 6a shows that BF region is the β phase with bcc structure. There are a large number of sub-grains with a size of about 80 nm, which are formed due to the dislocation movement after cold rolling. From Fig. 6c – 6d, it can be concluded that the hcp-structured α' martensite precipitates in the microstructure of the alloy after cold rolling with 60% reduction. The diffraction pattern of the α' phase shows a ring-shaped pattern, indicating the presence of many nanoscale small grains with different orientations inside the α' phase. This indicates that a large number of dislocations pass through the α' phase during the cold rolling process and small grains form in the α' phase. During the cold rolling process, titanium alloys with a near β shape generally produce α'' martensite phase with orthogonal structure. However, the reason for the formation of hexagonal martensite phase in this experiment may be the transformation from orthogonal martensite phase to hexagonal martensite phase during the cold rolling process. The formation of martensite phase will increase the hardening rate during cold rolling and the dislocation density, which can hinder the growth of grains during annealing to refine the grains after annealing[24].

Fig. 7 shows the microstructure of the annealed alloy after aging at 520–580 °C/2–8 h, as well as the corresponding XRD patterns and SEM images after different aging treatments. Fig.7d shows XRD patterns after aging at 520–580 °C for 4 h. It can be seen that there are hcp-structured α and bcc-structured β phases after aging at 550 °C and 580 °C, while in the microstructure after aging at 520 °C/4 h, in addition to α and β phases, there are also ω phases. From OM images of the alloy after different aging treatments in Fig. 7, it can be seen that with the increase in aging temperature and time, the

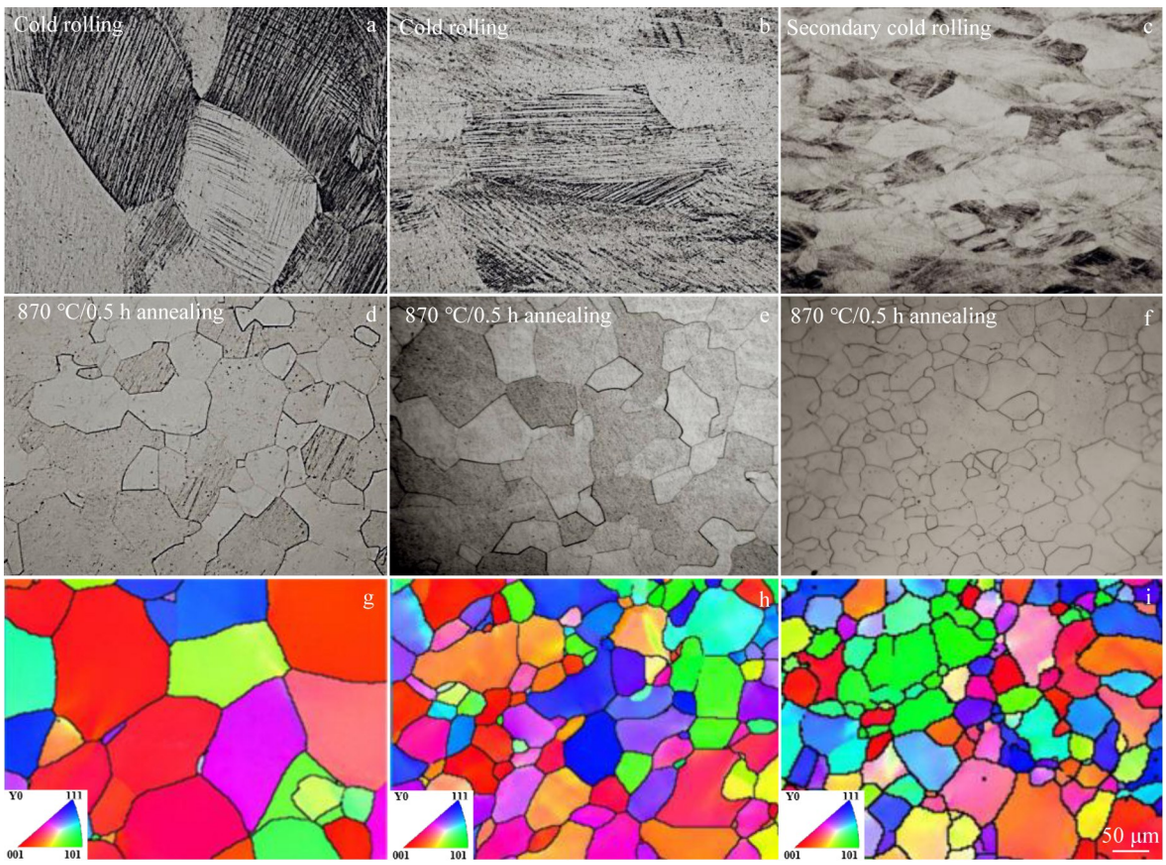

Fig.5 OM images after cold rolling (a–c), recrystallization (d–f), and IPFs (g–i) after annealing at 870 °C/30 min with different cold rolling reductions: (a, d, g) 30%; (b, e, h) 60%; (c, f, i) secondary 60%

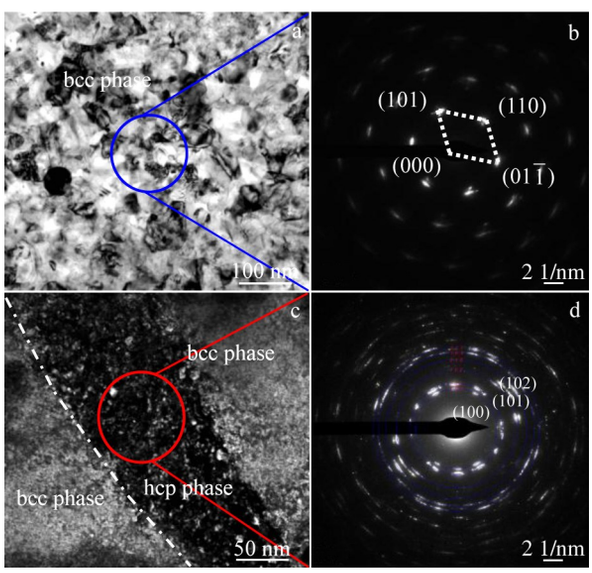

Fig.6 TEM images and corresponding SAED patterns of the alloy after cold rolling with 60% reduction: (a) BF image; (b) SAED pattern corresponding to the blue circle area in Fig.6a; (c) DF image; (d) SAED pattern corresponding to red circle area in Fig.6c

distribution of α phase becomes more uniform, and the size of α phase gradually increases. After 550 °C/8 h, the distribution of α phase in the microstructure is uniform, whereas the distribution of α phase is not uniform at other aging durations, and there are precipitation-free zones between grains.

Therefore, in order to ensure the uniform distribution of α phase, the aging treatment for this experiment is conducted at 550 °C/8 h. Fig.7b and Fig.7c show SEM images of the alloy after aging at 520 and 550 °C for 8 h, respectively. It can be seen that the α phase after aging at 520 °C shows a triangular distribution, while the α phase after aging at 550 °C shows a V-shaped distribution.

In order to further demonstrate the microstructure of the α phase after aging at 550 °C/8 h, the aged alloy was further characterized by TEM. Fig. 8 shows TEM BF image, high-resolution TEM (HRTEM) image, and strain distribution corresponding to HRTEM image of the alloy after aging treatment at 550 °C/8 h. It can be seen that a large amount of white α phases with a width of about 40 nm precipitate from three directions in the microstructure of the alloy after aging. Fig. 8b shows HRTEM image in the local region and corresponding fast Fourier transform image in the upper right corner. From Fig.8, it can be seen that α phase atomic arrangement is different in the local region, and there is significant lattice distortion between α phases with different orientations. The corresponding strain distribution map is highlighted.

Fig. 9 shows the tensile performance curves and corresponding hardening rate curves of the alloy after rolling,

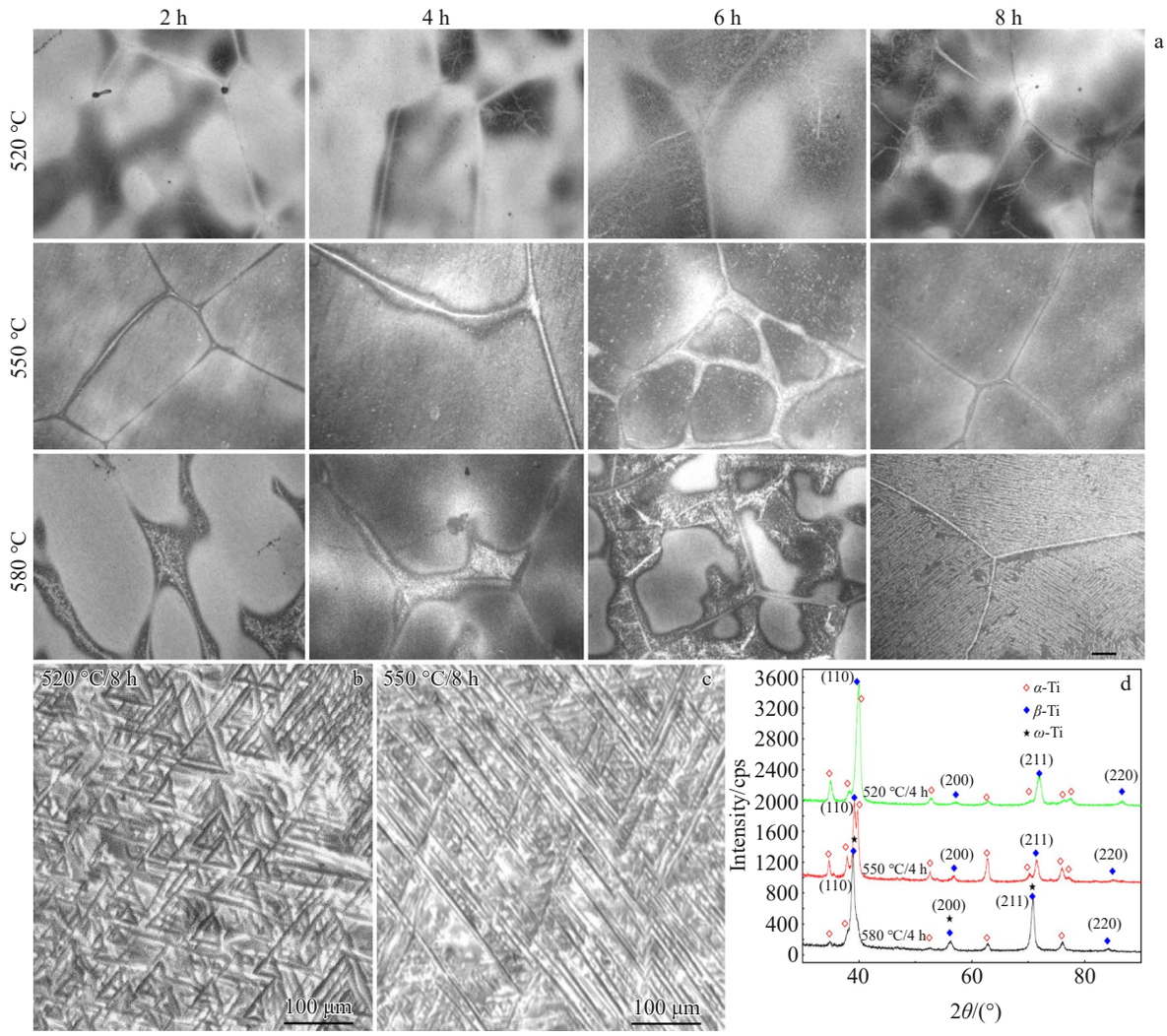

Fig.7 OM images of annealed alloy after aging at 520–580 °C/2–8 h (a); SEM images after aging at 520 °C/8 h (b) and 550 °C/8 h (c); XRD patterns of the alloy after different aging treatment (d)

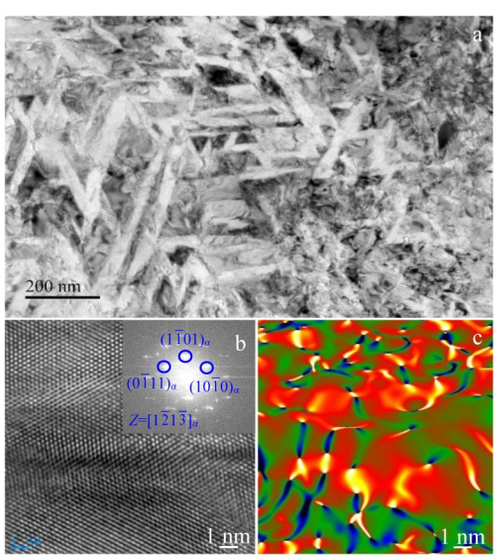

Fig.8 TEM BF image (a) and HRTEM image (b) of the alloy after aging treatment at 550 ° C/8 h; strain distribution diagram corresponding to Fig.8b (c)

annealing and aging treatments. It can be seen that the yield strength of the alloy with a single bcc structure after a single 60% reduction and single cold rolling and annealing (SCRA) reaches 900 MPa, while the elongation is 14%. The yield strength of the alloy after a second cold rolling and annealing (DCRA) with 60% reduction reaches 1050 MPa, which is 150 MPa higher than that of SCRA. However, the hardening rate curves indicate that the hardening rates of DCRA are not significantly different. Compared to the already applied Ti-10V-2Fe-3Al alloy, the alloy obtains higher strength after annealing. In addition, the alloy can achieve a yield strength of nearly 1400 MPa while still maintaining an elongation of 7% after a single cold rolling, annealing and aging (SCRAA) at 550 ° C/8 h. The yield strength of the alloy after intermediate annealing during cold rolling and aging (DCRAA) at 550 °C/8 h is close to 1500 MPa, while maintaining an elongation of about 5%. And the alloy after DCRAA has a high hardening rate in the initial deformation stage. The yield strength of the alloy after DCRAA is higher than that of the SCRAA. This is due to not only the strengthening effect of

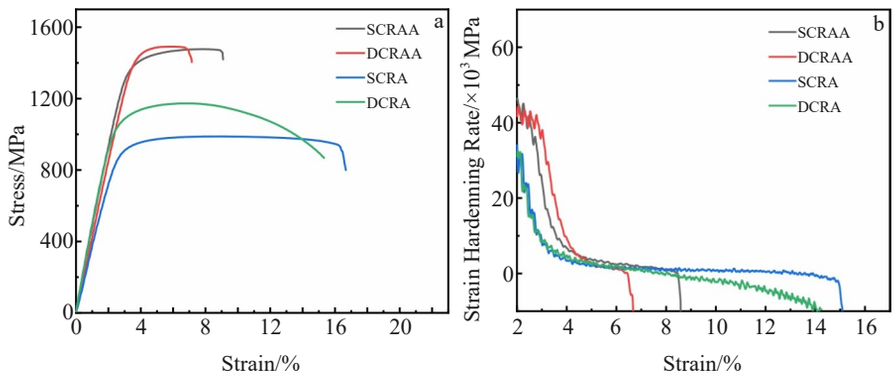

Fig.9 Stress-strain curves (a) and strain hardening rate curves (b) of the alloy after different heat treatments

finer grains obtained after secondary cold rolling and recrystallization, but also the influence of stress and thermal effects. The diffusion of elements in the alloy after secondary cold rolling and recrystallization is more complete and uniform, which will be beneficial to the strength and plasticity of the alloy.

Fig. 10 shows the tensile fracture morphologies of the alloy after SCRAA and DCRAA. For SCRAA alloy, the fracture features consist of cleavage platforms and dimples. It can be seen that there are obvious tearing edges on the cleavage surface in Fig. 10b. DCRAA alloy has fewer cleavage fracture platforms in its fracture morphology compared with SCRAA, which is mainly composed of dimples formed at the interface between α particles and β matrix. These dimples are relatively shallow compared to the dimples of SCRAA alloy, and absorb relatively less energy during the fracture process, which can result in lower fracture toughness of DCRAA alloy compared to SCRAA alloy.

4 Discussion

The yield strength of titanium alloy after annealing is contributed to the lattice resistance, solid solution strengthening, dislocation strengthening and grain boundary strengthening of the alloy. After aging, the yield strength of the alloy also exhibits precipitation strengthening on the basis of the strength of the solid-solution-treated alloy, as follows:

$$\sigma_{YS} = \sigma_0 + \sigma_{ss} + \sigma_{gb} + \sigma_p \quad (5)$$

where σ_{YS} is the yield strength of the alloy; σ_0 is the lattice resistance of the alloy; σ_{ss} and σ_{gb} are the contribution of solid solution strengthening and grain boundary strengthening, respectively; σ_p is the contribution of precipitation strengthening. The yield stress of the alloy without strengthening mechanism is as follows:

$$\sigma_0 = \sum_{i=1}^{n} C_i \sigma_{0i} \quad (6)$$

where C_i and σ_{0i} represent the molar fraction and yield stress of component i in the solid solution, respectively. After calculation, the lattice friction resistance of the alloy is 260 MPa. Solid solution strengthening can be described as follows:

$$\sigma_{ss} = AG\left[\sum_i \varepsilon_i^2 X_i\right]^{2/3} \quad (7)$$

where A is the fitting constant obtained by comparing calculated data with actual data, as shown in Table 2; G is the average shear modulus of the alloy, $G = \sum_i X_i G_{ii}^{(0)}$, where X_i is the atomic fraction of component i in the alloy and $G_{ii}^{(0)}$ is the shear modulus of pure i-component; $\varepsilon_i = (\eta_i'^2 + \alpha^2\delta_i^2)^{1/2}$, where α depends on the type of dislocation undergoing plastic deformation. Screw dislocations are usually taken as $3<\alpha<16$, and edge dislocations are taken as $\alpha>16$. The value is shown in Table 2. $\eta_i' = \dfrac{\eta_i}{1 + 0.5|\eta_i|}$. $\eta_i = \dfrac{1}{G}\dfrac{dG}{dX_i}$, which is a mismatch in elastic modulus, as follows:

$$\eta_i = p\sum_j X_j \delta G_{ij} \quad (8)$$

where p is the coefficient (for fcc structure, p=12/13; for bcc

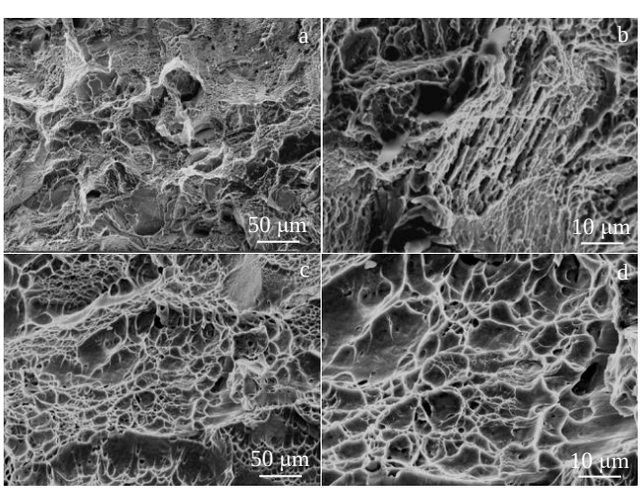

Fig.10 Tensile fracture morphologies of SCRAA (a–b) and DCRAA (c–d) samples

Table 2 Parameters of different strengthening models

Parameter	A	K/MPa·m$^{-1/2}$	K_s/MPa·μm^{-1}	α
Value	0.03596	0.4	285	10

structure, p=9/8); $\delta G_{ij}=\frac{2(G_{ii}^{(0)}-G_{jj}^{(0)})}{G_{ii}^{(0)}+G_{jj}^{(0)}}$; $\delta_i=\frac{1}{S_{\text{lat}}}\frac{d_{S_{\text{lat}}}}{d_{X_i}}$ is an atomic size mismatch, where S_{lat} is the average distance between the nearest atoms in a multicomponent alloy with atomic size mismatch. δ_i can be expressed by the following formula:

$$\delta_i=p\sum\nolimits_j X_j\delta R_{ij} \tag{9}$$

where $\delta R_{ij}=\frac{2(R_{ii}-R_{jj})}{R_{ii}+R_{jj}}$, $R_{ii}=s_{ii}^{(0)}/2$ and $s_{ii}^{(0)}$ is the distance between the nearest equilibrium atoms in the lattice of pure component i. The formula R_{ii} is only valid for alloys with the same lattice type. Correction is required for pure metal elements with different lattices, $R_{ii}=s_{ii}/2$, where s_{ii} is the average distance between the nearest atoms of component i in a multi-component alloy lattice, which is effective for different types of lattices. Parameters $K_{\text{lat}}^{(s)}$ and $S_{\text{lat}}^{(s)}$ can be considered as approximate values of the bulk modulus and average distance between atoms of the multicomponent alloy, respectively.

$$S_{ii}=\frac{K_{ii}^{(s)}S_{ii}^{(s)2}+K_{\text{lat}}^{(s)}S_{\text{lat}}^{(s)2}}{K_{ii}^{(s)}S_{ii}^{(s)}+K_{\text{lat}}^{(s)}S_{\text{lat}}^{(s)}} \tag{10}$$

$$K_{ii}^{(s)}S_{ii}^{(s)}=2m_{\text{lat}}n_{\text{lat}}f_{\text{lat}}{}^3[X_iK_{ii}^{(0)}S_{ii}^{(0)}/(m_i^{(0)}n_i^{(0)}f_i^{(0)3})] \tag{11}$$

$$K_{ii}^{(s)}S_{ii}^{(s)2}=2m_{\text{lat}}n_{\text{lat}}f_{\text{lat}}{}^3\left[\frac{X_iK_{ii}^{(0)}S_{ii}^{(0)2}}{m_i^{(0)}n_i^{(0)}f_i^{(0)3}}\right] \tag{12}$$

$$K_{\text{lat}}^{(s)}S_{\text{lat}}^{(s)}=m_{\text{lat}}n_{\text{lat}}f_{\text{lat}}{}^3\sum\nolimits_i\frac{X_iK_{ii}^{(0)}S_{ii}^{(0)}}{m_i^{(0)}n_i^{(0)}f_i^{(0)3}} \tag{13}$$

$$K_{\text{lat}}^{(s)}S_{\text{lat}}^{(s)2}=m_{\text{lat}}n_{\text{lat}}f_{\text{lat}}{}^3\sum\nolimits_i\frac{X_iK_{ii}^{(0)}S_{ii}^{(0)2}}{m_i^{(0)}n_i^{(0)}f_i^{(0)3}} \tag{14}$$

For bcc structure: $m_{\text{lat}}=m_i^{(0)}=8$, n_{lat}=2, $f_{\text{lat}}=\sqrt{3}/2$, $n_i^{(0)}=2$ and $f_i^{(0)}=\sqrt{3}/2$. After calculation, the solid solution strengthening contribution of the alloy is 508 MPa, and the influence of grain size on the strength of the aged alloy is relatively small, but it has a significant impact on the toughness of the alloy. The correlation between grain size and alloy strength can also be directly observed through Hall-Petch equiation:

$$\sigma_{\text{gb}}=Kd^{-1/2} \tag{15}$$

where K is the coefficient, and the value is shown in Table 2; d is the grain size. After calculation, the contribution of fine grain strengthening to the alloy is 65 MPa.

$$\sigma_{\text{p}}=\frac{K_{\text{s}}}{L_{\text{s}}} \tag{16}$$

where L_{s} is the spacing between secondary α phase particles, which can be obtained from the statistical graph of binary treatment based on SEM results in Fig. 11a; K_{s} is a fitting parameter, which is shown in Table 2. The average spacing of α phase in the microstructure after 550 °C/8 h aging is 0.648 μm. After calculation, the contribution of aging strengthening at 550 °C/8 h is 440 MPa.

Fig. 12 shows the strengthening composition diagram of the alloy. It can be seen that solid solution strengthening and precipitation strengthening are the main strengthening methods of the alloy. The contributions of lattice resistance and grain boundary strengthening are relatively small, and the total calculated strength differs little from the theoretical value.

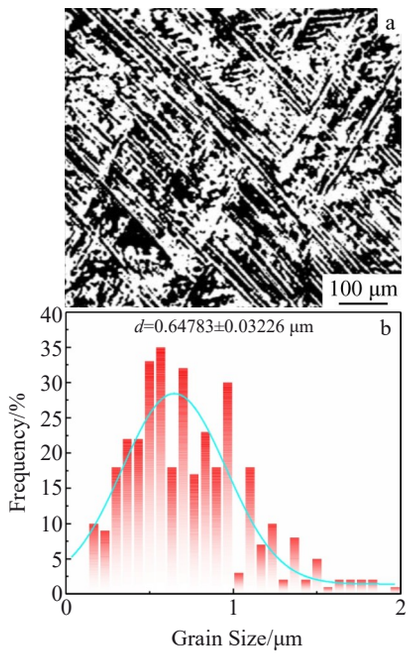

Fig.11 SEM image of alloy after aging at 550 °C/8 h (a); binary processing diagram based on SEM result in Fig.11a (b)

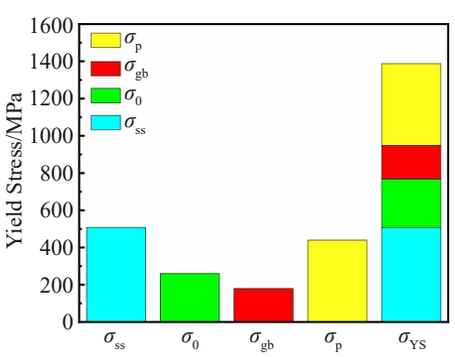

Fig.12 Strengthening composition diagram of alloy

5 Conclusions

1) A Ti-5.5V-4Mo-2.2Cr-Fe-3.6Al near β-type alloy was designed based on electron concentration, $[\text{Mo}]_{\text{eq}}$, and B_{o}-M_{d} values. The $[\text{Mo}]_{\text{eq}}$ of the alloy is a critical value of 10, and the position of the (B_{o}, M_{d}) value in the B_{o}-M_{d} diagram shows that the alloy undergoes martensitic transformation during deformation.

2) XRD and TEM results indicate that there is martensitic transformation in the microstructure of the alloy after 60% cold rolling. Due to the presence of martensite, the alloy obtains finer grain size after annealing and recrystallization during rolling process. EBSD grain statistics show that the grain size of the alloy after intermediate annealing in second

rolling process is 38 μm. The tensile results indicate that the yield strength of the alloy with a single bcc structure after intermediate annealing in second rolling process is 1050 MPa, with an elongation of 15%.

3) The microstructure of the alloy after aging at 550 °C/8 h is relatively uniform, with a yield strength of 1500 MPa and an elongation of 5%. The strength of the alloy is simulated and calculated using different models, and the error between the result of the aged alloy at 550 °C/8 h and the experimental results is small.

References

1 Li Jiaqi, Zhang Duyao, Chen Xiaobo *et al*. *Journal of Materials Science & Technology*[J], 2023, 166: 21

2 Tong Yanlin, Hua Ke, Sun Linghong *et al. Journal of Materials Science & Technology*[J], 2024, 196: 200

3 Gao Yipeng, Zheng Yufeng, Fraser Hamish *et al. Acta Materialia*[J], 2020, 196: 488

4 Wang X Q, Zhang Y S, Han W Z. *Acta Materialia*[J], 2022, 227: 117686

5 Li Tong, Kent Damon, Sha Gang *et al. Acta Materialia*[J], 2016, 106: 353

6 Zhang Tianlong, Wang Dong, Wang Yunzhi. *Acta Materialia*[J], 2020, 196: 409

7 Qiu Fucheng, Cheng Tuo, Song Yuchao *et al. Journal of Materials Science & Technology*[J], 2024, 171: 24

8 Chamanfar A, Huang M F, Pasang T *et al. Journal of Materials Research and Technology*[J], 2020, 9(4): 7721

9 Huang Feiyu, Huang Chaowen, Zeng Hongtao *et al. Journal of Materials Research and Technology*[J], 2023, 26: 7425

10 Starck L F, Sangali M, De Melo M F C *et al. Materials Letters*[J], 2023, 351: 134968

11 Zhang Qifei, Yang Shuai, Liu Shujun *et al*. *Rare Metal Materials and Engineering*[J], 2022, 51(7): 2645

12 Wang Wenting, Li Pei, Sun Qiaoyan *et al*. *Rare Metal Materials and Engineering*[J], 2020, 49(5): 1707

13 Ghorbani H R, Masallanejad M H, Atapour M *et al. Journal of Materials Research and Technology*[J], 2022, 20: 180

14 Hua Ke, Zhang Yudong, Kou Hongchao *et al. Acta Materialia*[J], 2017, 132: 307

15 Sadeghpour S, Abbasi S M, Morakabati M *et al. Scripta Materialia*[J], 2018, 145: 104

16 Zhang Changjiang, Jiang Xi, Lv Zhidan *et al. Transactions of Nonferrous Metals Society of China*[J], 2022, 32(4): 1159

17 Gu B, Chekhonin P, Xin S W *et al. Journal of Alloys and Compounds*[J], 2021, 876: 159938

18 Zhang C L, Bao X Y, Zhang D D *et al. International Journal of Plasticity*[J], 2021, 147: 103126

19 Li Jinguang, Zhang Keren, Hu Rui et al. *Journal of Materials Research and Technology*[J], 2024, 28: 4177

20 Coffigniez M, De Breuck P P, Choisez L *et al. Materials & Design*[J], 2024, 239: 112801

21 Zhang Feng, Feng Jun, Xiang Wei *et al. Materials Characterization*[J], 2024, 208: 113632

22 Wang Jie, Bai Shuxin, Tang Yu *et al. Journal of Alloys and Compounds*[J], 2021, 868: 159190

23 Marteleur M, Sun F, Gloriant T *et al*. *Scripta Materialia*[J], 2012, 66(10): 749

24 Zhao G L, Wen G, Song Y *et al. Materials Science and Engineering C*[J], 2011, 31: 106

通过成分设计和轧程中间退火工艺获得高强度近β型钛合金的研究

姜诗慧[1]，邸金南[2]，徐再东[3]，孙赛华[3]，毛萍莉[1]

(1. 沈阳工业大学 材料科学与工程学院，辽宁 沈阳 110870)

(2. 辽宁轨道交通职业学院，辽宁 沈阳 110230)

(3. 东北大学，辽宁 沈阳 110000)

摘　要：基于临界成分的多元合金化原则，结合电子浓度、钼当量和B_o-M_d等衡量β相稳定性的参数设计了一种近β型Ti-5.5V-4Mo-2.2Cr-Fe-3.6Al合金。对均匀化处理后的试样进行轧程中间退火处理，最后对合金进行时效处理。利用光学显微镜、扫描电子显微镜、X射线衍射仪、背散射电子衍射和透射电子显微镜等技术分析合金在不同状态下的组织，同时对合金的室温拉伸性能进行测试。结果表明，在轧制过程中合金发生马氏体相变，由于马氏体具有阻碍晶界迁移的作用，经过轧程中间退火后的合金获得了极其细小的晶粒组织。中间退火后合金的晶粒度为38 μm，晶粒细化使得退火处理后的合金具有良好的强塑性匹配，屈服强度达到1050 MPa，同时延伸率达到15%。经过时效处理后合金的组织中析出了大量细小而弥散的α相，细小α相的析出进一步提高了合金的性能，使合金强度突破1500 MPa并具有5%的延伸率。

关键词：近β型钛合金；冷轧；退火；拉伸性能

作者简介：姜诗慧，女，1989年生，博士，沈阳工业大学材料科学与工程学院，辽宁 沈阳 110870，E-mail：jiangshihui@sut.edu.cn